Formation of the Leading-edge Vortex and Spanwise Flow on an Insect-like Flapping-wing throughout a Flapping Half Cycle

N. Phillips
nathan.phillips@zoo.ox.ac.uk
and K. Knowles
k.knowles@cranfield.ac.uk
Aeromechanical Systems Group
Cranfield University
Defence Academy of the UK, Shrivenham, SN6 8LA, UK
nathan.phillips@zoo.ox.ac.uk

Abstract

This paper presents an experimental investigation of the evolution of the leading-edge vortex and spanwise flow generated by an insect-like flapping-wing at a Reynolds number relevant to flapping-wing micro air vehicles (FMAVs) ($Re =\sim 15000$). Experiments were accomplished with a first-of-its-kind flapping-wing apparatus. Dense pseudo-volumetric particle image velocimetry (PIV) measurements from $18\% - 117\%$ span were taken at twelve azimuthal positions throughout a flapping half cycle. Results revealed the formation of a primary leading-edge vortex (LEV) which saw an increase in size and spanwise flow (towards the tip) through its core as the wing swept from rest to the mid-stroke position where signs of vortex breakdown were observed. Beyond mid-stroke, spanwise flow decreased and the tip vortex grew in size and exhibited a reversal in its axial direction. At the end of the flapping half cycle, the primary LEV was still present over the wing surface, suggesting that the LEV remains attached to the wing throughout the entire flapping half cycle.

Nomenclature

$\bar{c}$ = mean chord length, m
CFD = computational fluid dynamics
CI = 95% confidence interval
f = flapping frequency, Hz
FMAV = flapping-wing micro air vehicle
LEV = leading-edge vortex
MAV = micro air vehicle
n = sample size
PIV = particle image velocimetry
Q = second invariant of ∇v, s^{-2} (see Equation 2)
r = length of one wing from root to tip, m
Re = mean Reynolds number ($\bar{V}_{tip}\bar{c}/\nu$)
S = symmetric part of ∇v, s^{-2}
T = flapping period $(1/f)$, s
v_z = z-wise velocity, m/s
∇v = velocity gradient tensor
$\bar{V}_{tip}$ = mean wingtip speed, m/s
xyz = coordinate system fixed to wing (see Fig. 1)
$x_{cam}y_{cam}z_{cam}$ = measurement coordinate system (see Fig. 3)
$X_IY_IZ_I$ = inertial coordinate system fixed to insect body (see Fig. 1)
α = mean angle-of-attack along span, deg (see Fig. 1)
α_{max} = maximum (most vertical) angle-of-attack along span, deg
α_{mec} = mechanism output angle-of-attack, deg
α_{mid} = mean angle-of-attack along span at mid-stroke, deg
α_{min} = minimum (most horizontal) angle-of-attack along span, deg
ν = kinematic viscosity, m^2/s
Ω = antisymmetric part of ∇v, s^{-2}
ϕ = stroke angle, deg (see Fig. 1)
ϕ_{cam} = measurement stroke angle, deg (see Fig. 3)
Φ = stroke amplitude, deg
σ = standard deviation
τ = rotation phase, $\%T$
θ = plunge angle, deg (see Fig. 1)
Θ = plunge amplitude, deg

1 Introduction

An autonomous airborne system that can operate indoors would be useful for many applications including indoor reconnaissance, search and rescue, and inspection in hazardous areas. Autonomous unmanned air vehicles (UAVs) and micro air vehicles (MAVs) including fixed- and rotary-wing MAVs exist for outdoor use, however, suitable systems for indoor use are relatively underdeveloped. This is because the requirements for this environment are extremely challenging, as they include high energy efficiency, and the abilities to operate at low flying speeds, sustain hover, and perform complex manoeuvres in confined spaces. As discussed in [1], the type of vehicle that would best meet these requirements would be a flapping-wing micro air vehicle (FMAV) which mimics the flight of two-winged insects (e.g. Diptera, Lepidoptera, Hymenoptera). Insects are seen in nature to possess the remarkable abilities to sustain hover and perform rapid and complex manoeuvres in confined spaces. In addition, this mode of flight is apparently efficient at low speeds [2] and is not susceptible to wall proximity effects as rotary-wing MAVs are. The motivation for developing FMAVs is to use them for indoor applications, as they show a particular suitability for this environment.

A hindrance in the development of FMAVs is the fact that many aspects of insect-like flapping-wing flight remain relatively unexplored and not well understood. One such aspect is how key flow structures, namely the lift-augmenting leading-edge vortex (LEV) produced by the flapping-wing, forms and decays throughout a flapping cycle. The formation of the LEV and the associated spanwise flow through its core have been the subject of a number of experimental studies. Ellington and his colleagues used flow visualisation with smoke on a mechanical model of a hawkmoth ($Re = 8000$) to observe the evolution of the LEV throughout a half-stroke and calculate the spanwise flow velocity through its core at select points [3, 4, 5]. The relation between the form of the LEV, its stability, and spanwise flow was the subject of an experiment performed by Birch & Dickinson in which PIV flowfield measurements were taken at the mid-stroke position on a mechanical model of a fruit fly wing ($Re = 160$) with and without flow-limiting fences [6]. Experiments on live hawkmoths by Bomphrey and his colleagues [7, 8] investigated the development of the LEV and measured its characteristics including velocity profiles using flow visualisation and PIV measurements.

As the flowfield generated by an insect-like flapping wing is highly three dimensional and time varying, it is of interest to extend the observations made by previous studies by obtaining more spatial and temporal detail of the LEV structure. This is achieved by performing many flowfield measurements spaced closely in time and space giving a high resolution three-dimensional picture of how the LEV forms and evolves. Probably the first study involving measurements of this

kind was that by Poelma et al. [9], which attempted to visualise and quantify the development of the flow around an entire $3D$ revolving wing throughout a flapping cycle. In this study, the authors performed phase-locked particle image velocimetry (PIV) measurements throughout an entire volume encompassing the wing (rather than a few planes), which was executing a simplified flapping motion at $Re = 256$ in a tank of oil. Measurements were taken at numerous points in time encompassing pitch reversal and the beginning of the upstroke, as well as for an impulsive start from rest to a quasi-steady state. Visualisation of the data focussed on the growth and shedding of spanwise vorticity formed at the leading and trailing edges. A similar study was performed by Lu and Shen [10] who performed dense PIV measurements along the span of a flapping wing for three points in time throughout a flapping cycle (before, at and after mid-stroke), where the wing operated at $Re = 1624$ in a water tank. They illustrated the development of spanwise flow and vortices between these measurement points. Given the limited number of studies of this kind, further investigation into the details of the development of the LEV and spanwise flow throughout a flapping cycle are required, particularly at a Reynolds number more relevant to FMAVs (Re on the order of 10^4).

The present work aims to investigate in spatial and temporal detail how the leading-edge vortex and spanwise flow generated by an insect-like flapping wing evolve throughout a flapping cycle at a Reynolds number relevant to FMAVs. The paper begins with the relevant background on insect flight and aerodynamic mechanisms (Section 2). An explanation of the experimental apparatus and setup is then given (Section 3) along with the flapping kinematics employed in this study (Section 4). The experimental procedure is given next (Section 5) followed by a description of the instantaneous wing position reconstruction method (Section 6). The routine used in the data processing is then described (Section 7) followed by an uncertainty analysis (Section 8). Finally, results are presented and discussed (Section 9) followed by conclusions (Section 10).

2 Insect Flight

2.1 Kinematics

The motion of an insect's wing can be broken down into four parts: downstroke, supination, upstroke and pronation (Fig. 1). Starting with the downstroke, this is the translation of the wing at a relatively constant angle of attack from its most aft and dorsal position to its most forward and ventral position. At the end of the downstroke supination occurs, which is when the wing rapidly comes to a stop and reverses its direction and angle of attack so that the wing's underside becomes the topside for the subsequent half stroke. The wing then translates with a relatively

constant angle of attack back to its most aft and dorsal position, which is referred to as the upstroke. Finally, at the end of the upstroke, the wing pronates, which is where it again rapidly comes to a stop and reverses its direction and angle of attack. Pronation and supination can be advanced or delayed by insects relative to stroke reversal to modulate aerodynamic forces [11]. The flapping frequency (f) of insect wings ranges from $5 - 200Hz$, and the path that the wingtip traces takes the form of irregular, self intersecting shapes typically resembling a figure-of-eight.

This paper only deals with insect flight during hover, thus, the insect's body is always considered fixed. The inertial $X_I Y_I Z_I$ frame (fixed to the earth) is aligned with the insect's body such that the X_I, Y_I, Z_I axes coincide with the insect's lateral (starboard), forward, and vertical directions respectively (Fig. 1). The additional xyz coordinate system illustrated in Fig. 1 is fixed to the wing (but does not pitch with the wing) such that the x axis is aligned with the wing's pitch axis, the y axis is always parallel to the $X_I Y_I$ plane and points forward, and the z axis is perpendicular to the two.

Upon observation of the phases of a flapping cycle, it is apparent that an insect's wing motion is composed of three separate motions: sweeping (fore and aft), plunging (up and down) and pitching (angle-of-attack variation). The position of the wing at any given moment is defined relative to the stroke plane (Fig. 1), which is considered parallel to the $X_I Y_I$ plane in the hover. After Willmott & Ellington [12], the angle from the X_I (lateral) axis to the projection of the wing's longitudinal axis (pitch axis) onto the stroke plane is the stroke angle ϕ, the angle between the minimum and maximum stroke angles throughout a flapping cycle is the stroke amplitude Φ, and the plunge angle θ is the position of the wing's longitudinal axis out of the stroke plane. In addition, the angle between the minimum and maximum plunge angles throughout a flapping cycle is the plunge amplitude Θ. The wing's geometric angle of attack relative to the stroke plane is the pitch angle α, with α_{mid} referring to the angle of attack at the mid-stroke position in the cycle. In both cases α is taken as the mean angle of attack along the span. Another kinematic parameter that should be mentioned is rotation phase, which describes the timing of pitch reversal with stroke reversal. Here it is defined as a percentage of the flapping period T, where a positive sign implies that pitching begins early, whereas a negative sign indicates that pitching is delayed. For example, at $20Hz$ flapping frequency a rotation phase of 5% means that the wing begins pitching early so that it reaches 90° angle of attack $2.5ms$ before reaching the end of the stroke.

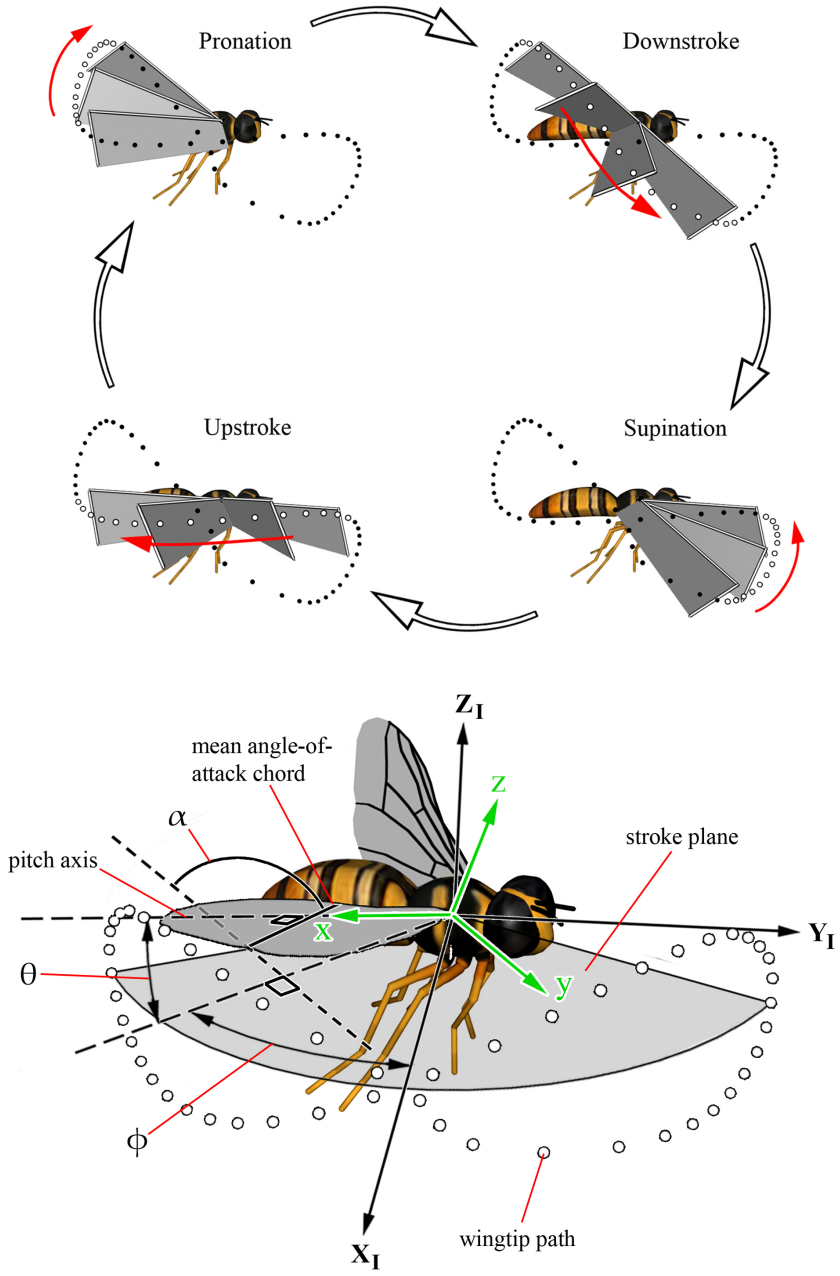

Figure 1: Flapping cycle (top), definition of kinematic parameters (bottom)

2.2 Aerodynamic Mechanisms

An insect's ability to produce lift values beyond predictions from steady state theory appears to be a result of several aerodynamic mechanisms. A number of these will be described here, including the leading-edge vortex (LEV) and spanwise flow. A detailed discussion on aerodynamic mechanisms relevant to insects may be found elsewhere [13, 14, 15, 16].

The most important aerodynamic mechanism relevant to insects is the leading-edge vortex (LEV). It was first observed by Maxworthy [17] on a pair of model insect wings where it was reported that as the wings swept, a 'separation-vortex' (the LEV) formed on the upper surface of each wing which developed a flow through its axis. Maxworthy realised that this axial flow prevented the LEV from shedding by transporting vorticity out into the tip vortex. In later years, the LEV was observed to form on the wings of a real hawkmoth and a mechanical model of a hawkmoth (the 'flapper') by Ellington and his colleagues [3]. They also reported the existence of a spanwise flow through the core of the LEV which was postulated to be a result of a pressure gradient from root to tip [3]. Such a pressure gradient was confirmed in computational studies by Wilkins [15, 18]. The LEV starts off small at the root and grows in size and strength towards the tip because of the increase in wing tangential velocity seen along the span from root to tip. The higher flow speeds (and hence lower pressures) near the wingtip induce a flow from the weaker (and relatively higher pressure) wing root end of the LEV. In agreement with Maxworthy, Ellington also suggested that this spanwise flow stabilises the LEV (which would normally rapidly grow in size and be shed into the wake) and keeps it attached by transporting vorticity from the LEV into the tip vortex. This has been confirmed in CFD studies performed by Wilkins [15, 18] who observed that on a two-dimensional translating wing, the LEV forms and sheds within the first three chord lengths of travel (when $Re > 25$), whereas a three-dimensional rotating wing (at low to moderate aspect ratio) forms an attached and stable LEV even at higher Reynolds numbers (Re of the order of 10^4). However, the stability of the LEV appears to vary as some experimental studies have shown that the LEV remains attached in general for revolving wings [19, 20], while others have shown that it continually forms and sheds [21, 22, 23]. Although the LEV is typically reported to have a conical structure, it has also been reported to be more cylindrical in shape and does not always have an extensive spanwise flow through its core [24, 7, 14].

3 Experimental Apparatus & Setup

3.1 'Flapperatus'

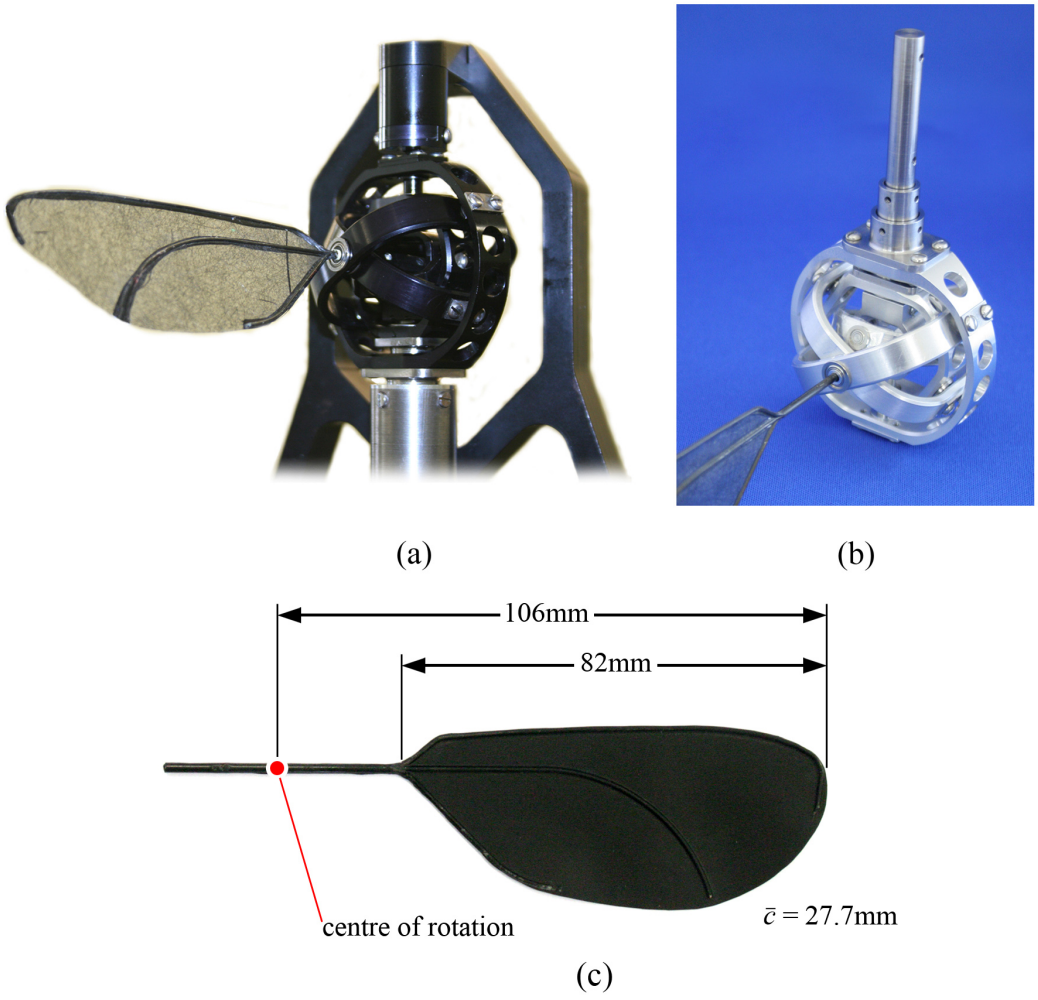

Figure 2: (a) closeup of flapperatus; (b) flapping mechanism; (c) wing planform

The mechanical flapper apparatus (the 'flapperatus') pictured in Fig. 2, enables an insect-like wing to be flapped with three controllable degrees of freedom (sweeping, plunging and pitching). It operates in air on the FMAV scale ($\sim 150mm$ wingspan) so that it experiences the true flow conditions that a real FMAV would experience. Variable flapping-wing kinematics up to a $20Hz$ flapping frequency are produced using a patent-pending, three-degree-of-freedom $3-\underline{R}RR$ parallel spherical mechanism. The mechanism has three concentric drive shafts

which are each coupled to a servo motor via $1:1$ cable drives. In addition, an encoder is mounted on each drive shaft so that the time-history of the actual flapping kinematics can be recovered since the relation between the drive shaft angles and wing position is known. The entire apparatus is mounted on a swivel and a traverse (Fig. 3) which permit measurement at different positions in the flapping cycle, and spanwise locations respectively by allowing the wing to be rotated and translated relative to the measurement plane. A custom programmed microcontroller (Parallax Inc., protoboard no. 32212) was used to monitor the drive shaft positions (via the encoders), trigger PIV data acquisitions at desired points in the flapping cycle, and control the traversing of the flapperatus. The flapperatus, and its flapping mechanism in particular, are described in greater detail elsewhere [25, 16].

The wing used on the apparatus for the present study (seen in Fig. 2) was the same wing designed and manufactured by Galiński and Żbikowski [26]. The planform shape of this wing originated from the 'four-ellipse' design of Pedersen [27], and was produced from four elliptic arcs with truncated areas near the root to accommodate mechanical limitations. As illustrated, the wing design consisted of three main spars made from carbon roving, with a membrane made of carbon mat. The wing length from root to tip was $82mm$, and the wingtip measured $106mm$ from the centre of rotation when mounted on the flapping mechanism. The mean chord length was $27.7mm$ and the wing area was $2270mm^2$. Further details on the wing design and manufacturing may be found elsewhere [26].

For the present experiment, the flapperatus was placed inside an hexagonal test chamber designed to isolate the experiment from outside disturbances and contain the seeding, whilst minimising wall interference effects. Inside the chamber the flapping wing was positioned over 15, 6 and 13 wing lengths (r) from the walls, ceiling and floor respectively.

3.2 PIV Setup

The PIV system utilised an angular set-up, rather than a translational set-up due to its greater out-of-plane accuracy [28, 29]. Here, the cameras were oriented as illustrated in Fig. 3 with the right camera viewing the measurement plane straight-on, and the left camera viewing at 48.5° from the normal with the CCD tilted with respect to the lens according to the Scheimpflug condition [30]. Here, the $x_{cam}y_{cam}z_{cam}$ frame is the coordinate system fixed to the PIV measurement system, and thus is the frame in which velocity components are measured. Also illustrated is the geometric relation between the inertial ($X_IY_IZ_I$) frame (fixed to the support structure), and the measurement ($x_{cam}y_{cam}z_{cam}$) frame, where they are separated by the measurement stroke angle ϕ_{cam} which sets the desired point in the flapping cycle to perform flowfield measurements. This angle is set with the

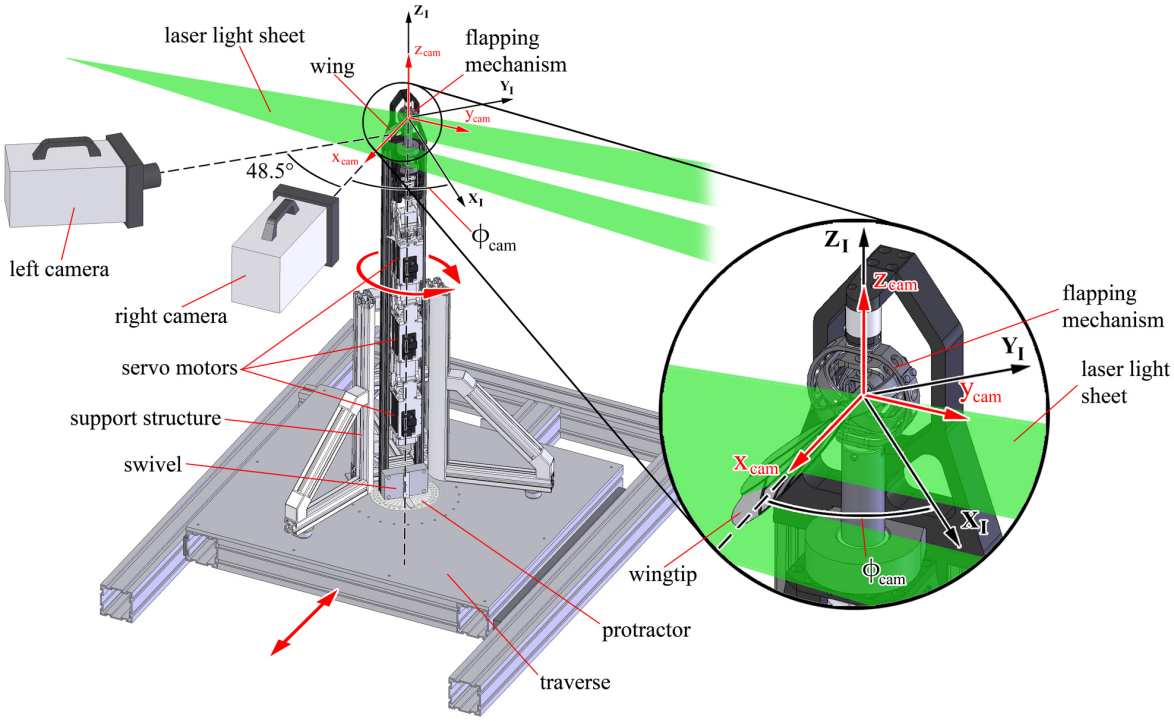

Figure 3: Schematic of experimental setup and relation between inertial $X_I Y_I Z_I$ (fixed to support structure) and measurement $x_{cam} y_{cam} z_{cam}$ frame fixed to PIV measurement system

aid of a protractor at the base of the flapperatus (Fig. 3), which is aligned such that when ϕ_{cam} and ϕ are both zero the wing is edge-on to the right camera when the wing is at rest. The cameras used were two PowerView^{TM} HS-3000 high-speed cameras (model 630064) with a resolution of $1024 \times 1024px^2$ from the Engineering & Physical Sciences Research Council equipment loan pool. A $60mm$ lens at an $f\#$ of 2.8, and a $105mm$ lens at an $f\#$ of 4 were used for the right and left cameras respectively. The laser light sheet was created with light sheet optics and a New Wave Research Gemini Nd:YAG double pulsed laser with a wavelength of 532 nm. The seeding used was smoke generated from a smoke machine using global mix smoke fluid by Le Maitre.

4 Flapping Kinematics

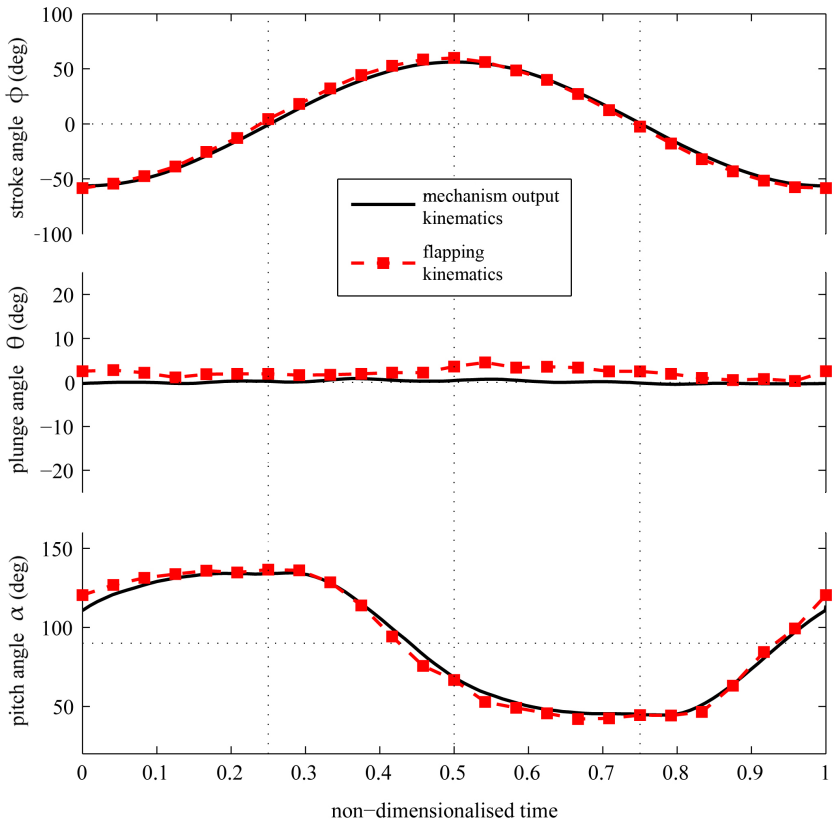

Figure 4: Flapping kinematics; $f = 20Hz$; $\Phi = 118.3°$; $\Theta = 4.2°$; $\alpha_{mid} = 43.3°$; rotation phase $= 6.2\%$; time is non-dimensionalised with respect to the flapping period T $(0.05s)$

The flapping kinematics employed in the present study were modeled after

simplified kinematics from Diptera, and are illustrated in Fig. 4. Here, the mechanism output kinematics are the kinematics demanded by the flapping mechanism, and the flapping kinematics are the actual kinematics of the wing accounting for wing flexion. If the wing were infinitely rigid then the flapping kinematics would match the mechanism output kinematics. Mechanism output kinematics were recovered using the recorded drive shaft angles (via encoders, see Section 3.1) and the known relation between the drive shaft and flapping kinematics. Details on this relation can be found in [16]. The method by which the actual flapping kinematics were recovered will be outlined in Section 6. The mechanism output kinematics are characterised by $f = 20Hz$, $\Phi = 112.7°$, $\Theta = 1.3°$, $\alpha_{mid} = 45.6°$, $\tau = 6.1\%$. However, as indicated, due to wing flexion the actual kinematics were $f = 20Hz$, $\Phi = 118.3°$, $\Theta = 4.2°$, $\alpha_{mid} = 43.3°$, $\tau = 6.2\%$. These kinematics gave a mean Reynolds number of $Re = 15210$.

The degree of torsional wing flexing along the span throughout the entire flapping cycle is given in Fig. 5. Here, the pitching kinematics from the bottom of Fig. 4 are re-plotted together with α_{min} and α_{max}, which refer to the most horizontal and most vertical local pitch angles respectively along the wing at an instant. Here, α_{max} occurs towards the root and α_{min} occurs towards the wingtip. These angles give an indication of wing twist, where the average twist along the span, defined here as the difference between α_{min} and α_{max} is $6.7°$ in the pitch-down direction. The pitch angle α is simply the mean pitch angle along the span, and α_{mec} is the mechanism output angle of attack (angle of attack demanded by the flapping mechanism).

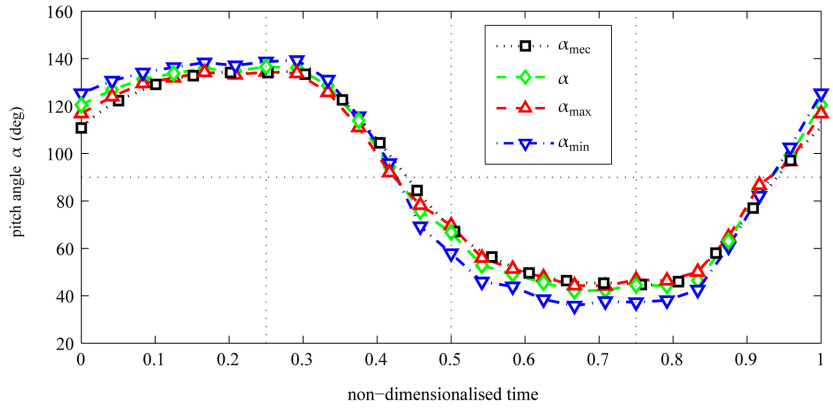

Figure 5: Comparison of mechanism output angle of attack (α_{mec}), mean (α), maximum (α_{max}) and minimum (α_{min}) angle of attack; time is non-dimensionalised with respect to the flapping period T $(0.05s)$

5 Experimental Procedure

For the present experiment, 12 azimuthal positions evenly spaced in time throughout a flapping half cycle were chosen as the measurement positions. The start of the flapping half cycle $0T$ (recall T is the flapping period) was taken as the time when the wing is at rest and about to accelerate into a half-stroke, as seen at $0T$ in Fig. 4. The measurement positions start at $0.04T$ and progress to $0.5T$ in increments of $T/12$. Measurements were performed for only a half cycle, rather than a full cycle, because the flows generated by half-strokes in opposite directions have been reported to be mirror images of each other [31] for symmetric kinematics (as used here). Only analysing half a flapping cycle was, therefore, deemed sufficient to describe what occurs for a full flapping cycle.

The first step in the experimental procedure was to rotate the flapperatus to the correct azimuthal position denoted by the measurement stroke angle ϕ_{cam} (e.g. see Fig 3) so that the right-hand camera would view the wing 'edge-on' at the desired measurement point in the flapping cycle. Smoke was then released into the test chamber and four minutes were allowed to elapse before beginning the experiment. As will be described in Section 8, this 'settle time' was observed to be appropriate to allow the seeder-induced flow to reduce to an acceptable level, and for the seeding density to become uniform. After this 'settle time', the flapperatus was ramped up to a $20Hz$ flapping frequency with the flapping kinematics illustrated in Fig. 4. Once the flapperatus reached its desired flapping frequency, 10 seconds (200 flapping cycles) were allowed to elapse, which was more than sufficient to surpass any start-up effects as merely 25 flapping cycles has been shown to be appropriate for such effects to diminish [16]. Next, starting from approximately 18% span where $\%$ span is defined from the wing root (located 24mm from the centre of rotation) to tip, 15 image pairs (for both cameras) were acquired using a pulse separation of $22\mu s$, for each of 81 spanwise locations extending up to 117% span, and spaced $1mm$ apart. The end result of this is a dense $3D$ grid of three-component velocity data for the given measurement position in the flapping cycle. As described in Section 3.1, changing the spanwise measurement position is accomplished by traversing the flapperatus with respect to the measurement plane. Here the flapperatus was traversed in $1mm$ increments between measurements, where 40 flapping periods were allowed to elapse following the arrival at a new measurement position before acquiring image pairs. The average and peak traversing speeds in this case were 0.002% and 0.01% of the mean wingtip speed ($8.4m/s$) respectively. Nevertheless, to verify that the act of traversing the flapperatus in this manner did not alter the flow, measurements taken with traversing were compared to measurements with no traversing for the same spanwise measurement location. The resulting vector maps showed no differences in the flowfield. To obtain a complete picture of the flowfield around the

entire wing, flowfield measurements underneath the wing were also performed at each measurement position, which were then combined with the other corresponding topside measurements.

6 Wing Position Reconstruction

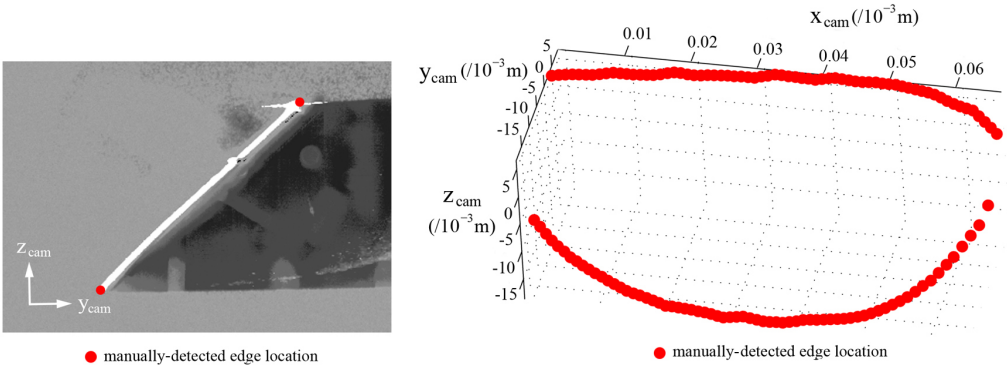

(a) (b)

Figure 6: Recovery of instantaneous wing position and flexion from raw images; (a) illustration of manual detection (red dots) of leading and trailing edge from raw image; (b) manually-detected edge locations (red dots) from all spanwise locations revealing instantaneous wing position and flexion

The acquired raw image pairs from the PIV data acquisition were also used to reconstruct the instantaneous wing position, flexion and the local geometric angle of attack along the span. This was accomplished by manually locating the leading- and trailing-edge positions in the raw images obtained during the PIV flowfield data acquisition, an example of which is given in Fig. 6a. This process was applied at every third spanwise measurement location, and the most tip-ward spanwise location that intersects the wingtip. The result is a collection of $3D$ points in the $x_{cam}y_{cam}z_{cam}$ measurement coordinate system defining the instantaneous form and position of the wing as illustrated in Fig. 6b. Leading- and trailing-edge points in between every third measurement location were inserted via interpolation. Such a method was also employed by Poelma et al. [9].

With the $3D$ coordinates of the wing edge obtained using the aforementioned method, a line representing the pitch axis can be constructed in this frame since the pitch axis lies a known distance from the leading edge. This then allows the instantaneous stroke, plunge and pitch angles of the wing to be recovered, giving the actual flapping kinematics. With the known orientation of the wing and its pitch axis in the measurement frame (i.e. Fig. 6b), and the fact that the geometric

relation between the measurement frame and inertial frame is known (from the ϕ_{cam} angle, see Fig. 3), then it follows that the orientation of the wing in the inertial frame, in which ϕ, θ, α are defined (see Fig. 1), can be determined. In addition, with the known orientation of the pitch axis in the measurement frame, the geometric relation between the measurement frame and the xyz frame fixed to the wing can then be determined. Further details on the employed wing position reconstruction technique can be found in [16].

7 PIV Processing & Analysis

Before image pairs were cross-correlated, reflections on the wing and in the background were removed by averaging the multiple samples of images taken at a given spanwise location for each exposure, and then subtracting these averages from each sample at the same measurement location. Image calibration was performed using a calibration plate with dots spread across two planes, which was aligned with the laser light sheet. Processing was performed with DaVis FlowMaster software by LaVision using an FFT-based cross-correlation algorithm with a Gaussian peak fit to locate correlation peaks to within sub-pixel resolution. An initial interrogation window size of $32 \times 32\ px^2$ was employed, which progressed to a final interrogation window size of $16 \times 16\ px^2$ with two passes and a 50% overlap. This resulted in an in-plane grid cell size of $1mm^2$. Deformed interrogation windows were also used which increases the number of matched particles and the signal-to-noise ratio. Between passes from the initial to final interrogation window size, the median filter proposed by Westerweel [32] was utilised to locate spurious vectors and replace them by interpolation. Registration error (see [33]) arising from slight misalignment between the laser light sheet and the calibration plate (which is unavoidable) was corrected using the approach based on a 'disparity map' [33, 34]. The resulting vector maps for a given measurement location were averaged, and then assembled into a $3D$ matrix representing the flow velocities throughout the measurement volume surrounding the wing with a spatial grid cell size of $1mm^3$.

As noted in Section 3.2, measured velocity components are in the $x_{cam}y_{cam}z_{cam}$ frame. These were transformed to the xyz frame using the known geometric relation between the two frames. Finally, the kinematic data obtained from the drive shaft encoders were used to determine the actual wing speeds at the measurement point. These were then used to convert the measured vectors from laboratory coordinates to wing coordinates (vectors with respect to the wing).

To identify the location of vortices in the flowfield, line integral convolution (LIC) [35] (which makes vortices more visible) was applied to every xy,yz, and xz plane in the measurement volume. With the resulting LIC images, approxi-

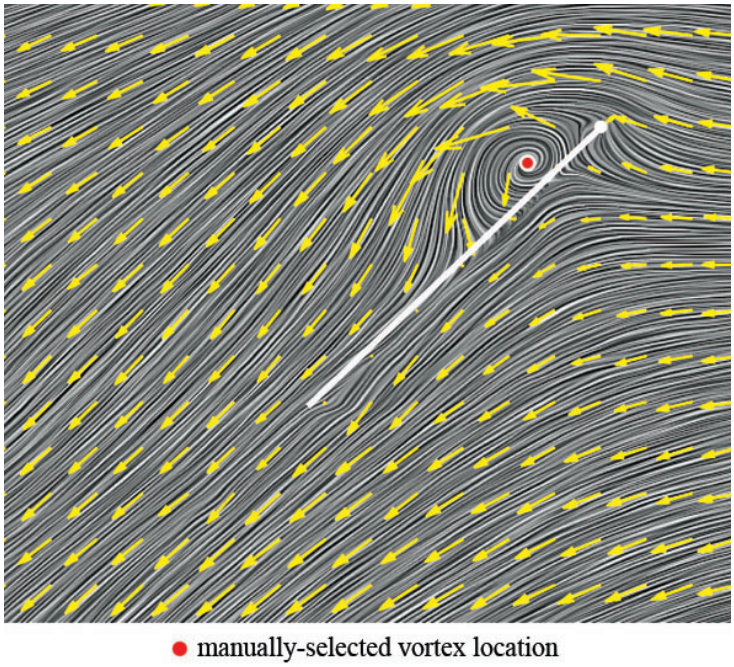

Figure 7: Example vector map (undersampled) overlaid on a LIC image illustrating manual selection of a vortex location (red dot)

mate vortex core locations were manually selected on every plane, an example of which is given in Fig. 7. The selected vortex core locations were then used as starting points from which to release instantaneous streamlines in order to make vortex structures visible. It should be noted that this was employed as a method of seeding the vortices with points from which to create streamlines, rather than a method for identifying the vortex axis. In addition, only starting, tip and leading-edge vortices were seeded in this manner as this study focuses on the development of these structures. Vortices underneath the wing shed from the previous stroke and small-scale Kelvin-Helmholtz vortices were ignored. To provide a secondary indication of the presence of vortex structures that was not dependent upon a user perspective, vortical structures were also identified using the Q criterion by Hunt et al. [36]. This criterion identifies vortices as areas where the second invariant Q, of the rate of deformation tensor ∇v is positive, where Q can be written as:

$$Q = (\| \Omega \|^2 - \| S \|^2)/2 \tag{1}$$

Here Ω and S are the antisymmetric and symmetric parts of ∇v respectively. This decomposition can be thought of as separating the local fluid motion into strain and shear rates, which are lumped together in S, and rigid-body-like rotation rates which are grouped into Ω. Thus, if at a given location Ω dominates over S,

then that region is a vortex since the local fluid motion will be dominated by rigid-body-like rotation.

8 Uncertainty Analysis

The first source of error considered is that that arises from an inadequately large sample size. The smaller the sample size, the further the averaged data will be from the true mean, and thus, have a larger error associated with this. To quantify this error a separate study was performed in which 100 samples were taken at 50% span at the mid-stroke point in the flapping cycle. At each point in the measurement grid, 95% confidence limits were computed for the measured velocities for sample sizes of $5 - 100$ using the standard formula for a 95% confidence limit for a normal distribution:

$$CI = \pm 1.96 \frac{\sigma}{n} \tag{2}$$

Here σ and n are the standard deviation and sample size respectively. The result for a given sample size is a 'map' of the 95% confidence limits at each point across the measurement plane. From this analysis, it was found that for the employed sample size of 15, the mean 95% confidence limit in the measurement area for a velocity measurement was 3.3% of the mean wingtip speed. Thus, with this sample size the vectors are on average $\pm 3.3\%$ of $\bar{V}_{tip}$ away from the true mean. Further details on this study may be found elsewhere [16].

Calibration error arises when the spatial measurement scales obtained with the calibration plate differ slightly from their true values. This error was found to be 0.2% on measured displacements, thus resulting in an error in velocity measurements that is also 0.2%.

Another error related to the calibration is error in the reconstruction of the $3D$ velocity components from slight misalignment between the calibration plate and the laser light sheet. This error was quantified numerically by calculating the misalignment based on the gradients in the disparity map as outlined in [34] and then computing the effect on the measured velocity components using the known geometry of the experimental setup. It was found that the error on velocity measurements was 1.9% of the mean wingtip speed. For more details on this analysis, the reader is referred to [16].

To ensure that measurements were not contaminated with flows generated in the act of filling the test chamber with smoke, a 'settle time' experiment was performed in which seeding was released (using a fixed burst length) and the resulting flow was measured using a pulse separation of $5ms$. After four minutes the flow settled to a level below $0.03m/s$ (approximately 0.4% of the mean wingtip speed),

which was deemed to be sufficiently low that subsequent experiments would not be contaminated. In addition, a test was performed to ensure that no recirculation formed in the test chamber as a result of running the flapping-wing for a prolonged period of time. The flowfield was measured on the flapping-wing at set intervals at the same spanwise location over a period of seven minutes (longer than an experimental run). Results revealed that no recirculation was present as the velocity components did not drift over time.

Errors in the PIV data processing were quantified using the approach described by Willert [37, 33], in which error is measured by processing particle image pairs where the particles have displaced by an amount that is known reliably. Using this approach, the flow was measured four minutes after a seeding burst (at which it was known that the flow velocity was below $0.03m/s$) using a short pulse separation of $4\mu s$. This short pulse separation in conjunction with a low flow velocity meant that the actual displacement of the particles between pulses was virtually zero. The captured image pairs were processed using the same method described in Section 7. The resulting displacements in conjunction with the pulse separation used in the experiment ($22\mu s$) revealed rms in-plane and out-of-plane errors of $0.18m/s$ and $0.19m/s$ respectively. These errors combine to a norm equal to 3.1% of the mean wingtip speed.

Adding all errors including those from the employed sample size, calibration error, $3D$ vector reconstruction error from calibration plate misalignment, unsettled flow, and PIV processing error, the total error on velocity measurements is found to be 4.9% of the mean wingtip speed.

9 Results & Discussion

In the following discussion, results are presented in the xyz frame fixed to the wing (see Fig. 1). Figure 8 illustrates top views (looking in the $-z$ direction) and root views (looking in the x direction) of the wing and the identified vortices for the first quarter of the flapping cycle, while Fig. 9 illustrates the same views for the second quarter of the flapping cycle. In both figures black instantaneous streamlines are released from the leading edge, tip and trailing edge, and instantaneous streamlines coloured with normalised spanwise velocity are released from points seeded in the vortices (as described in Section 7). Here spanwise velocity is normalised with respect to the mean wingtip speed ($8.4m/s$). Lastly, transparent iso-surfaces of $Q = 6 \times 10^6 s^{-2}$ are shown by the dark grey regions (only in the top views) to provide a secondary indication of the presence of vortical structures. This threshold for Q was chosen because it successfully identified vortical structures while avoiding most of the effects from noise, as plotting all areas where $Q > 0$ was found to saturate the measurement volume due to noise in the ve-

locity measurements. Chordwise vector maps overlaid on LIC images coloured with spanwise velocity normalised with respect to the mean wingtip speed are also shown in Fig. 10 for 25%, 50% and 75% span at five points throughout the flapping half cycle. The vector maps in this figure are undersampled such that only every fourth vector in the grid is shown.

As illustrated in Figs 8 and 10, immediately after the start of the flapping half cycle at $0.042T$, a starting vortex is clearly visible at the outboard section of the trailing edge, along with a starting tip vortex. At this time, the LEV has also started to form at the leading edge towards the tip, and spanwise flow through the core of the LEV is already present. The LEV from the previous half-stroke can also be seen at this time in the root view underneath the wing towards the leading edge in Fig. 8. This is highlighted by the fact that the black instantaneous streamlines released from the leading edge inboard of approximately 40% span curl underneath the wing in the same sense as the LEV from the previous half-stroke. This previous LEV is also clearly visible at the most root-ward section in Fig. 10.

At $0.08T$ the rest of the trailing-edge starting vortex has been shed at the inboard sections of the wing. In addition, the tip vortex and LEV have grown in size and the level of spanwise flow through the core of the LEV has increased. At this time, the LEV from the previous half-stroke is still present underneath the wing, but has moved further downstream towards the trailing edge since $0.042T$.

Beyond $0.083T$ the starting vortex is left behind in the wake and the LEV continues to grow in size and strength with an increasing spanwise flow through its core, reaching a peak of approximately two times the mean wingtip speed at mid-stroke ($0.25T$). The dark grey iso-surfaces of $Q = 6 \times 10^6 s^{-2}$ reinforce the location of the core of the LEV, and also suggest the presence of a smaller secondary LEV present right along the leading edge, which appears to form between $0.083T$ and $0.125T$ when the core of the first LEV shifts towards the trailing edge. These aft and forward LEVs will be referred to as the primary and secondary LEV respectively. The presence of two leading-edge vortices has been reported previously on live butterflies by Srygley $\&$ Thomas [38] and also on a mechanical flapping wing by Lu et al. [31].

At $0.208T$ it can be seen that the normalised spanwise flow through the core of the primary LEV suddenly drops from approximately 1 to 0.5 around 65% span, after which the instantaneous streamlines spiral towards the tip with a larger radius, indicating that the vortex core diameter has increased. This effect becomes even more pronounced as the sweep progresses to $0.25T$, where the sudden drop in spanwise flow has shifted slightly towards the root, beyond which the vortex diameter has grown even larger. The sudden increase in vortex diameter seen at $0.208T$ and $0.25T$ is an indication of vortex breakdown (also known as vortex burst). Breakdown of the LEV was also reported to occur around mid-stroke at

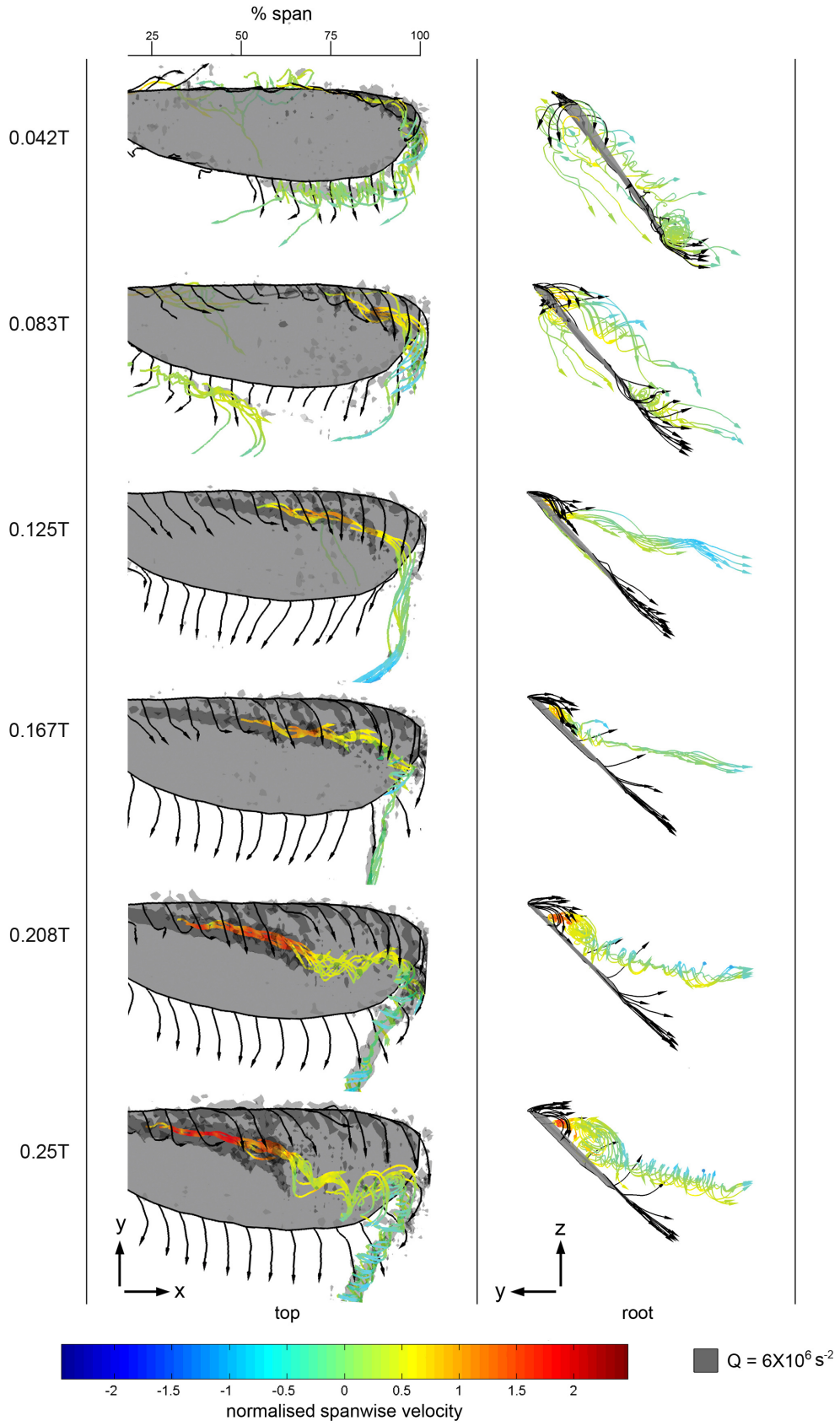

Figure 8: Top and root views illustrating the formation of vortices and spanwise flow throughout the first quarter of the flapping cycle; black arrows indicate instantaneous streamlines released along the wing edge; coloured instantaneous streamlines are released from vortex cores, and are coloured with spanwise velocity normalised with respect to the mean wingtip speed; dark grey areas indicate iso-surfaces of $Q = 6 \times 10^6 s^{-2}$

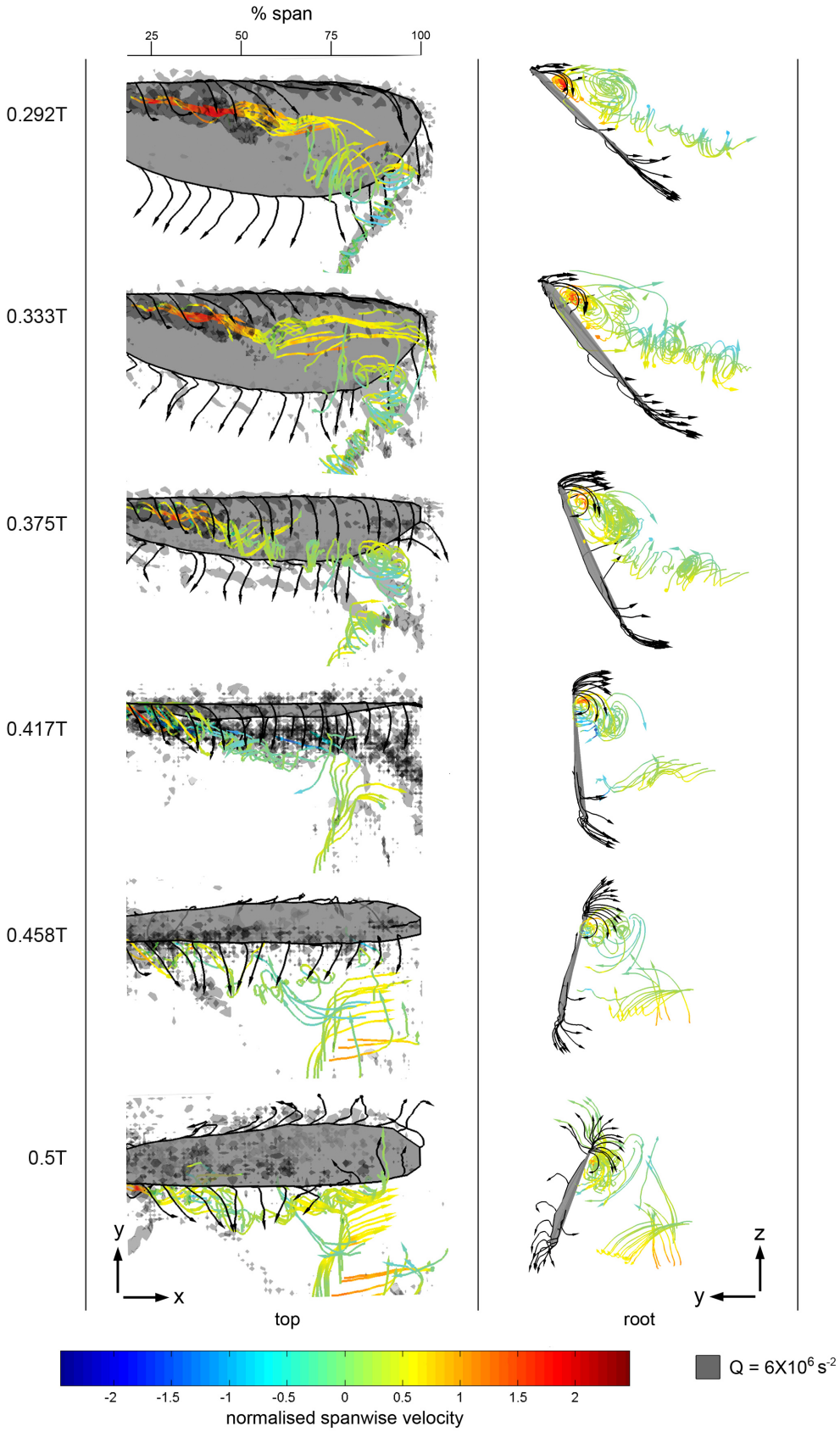

Figure 9: Top and root views illustrating the formation of vortices and spanwise flow throughout the second quarter of the flapping cycle; black arrows indicate instantaneous streamlines released along the wing edge; coloured instantaneous streamlines are released from vortex cores, and are coloured with spanwise velocity normalised with respect to the mean wingtip speed; dark grey areas indicate iso-surfaces of $Q = 6 \times 10^6 s^{-2}$

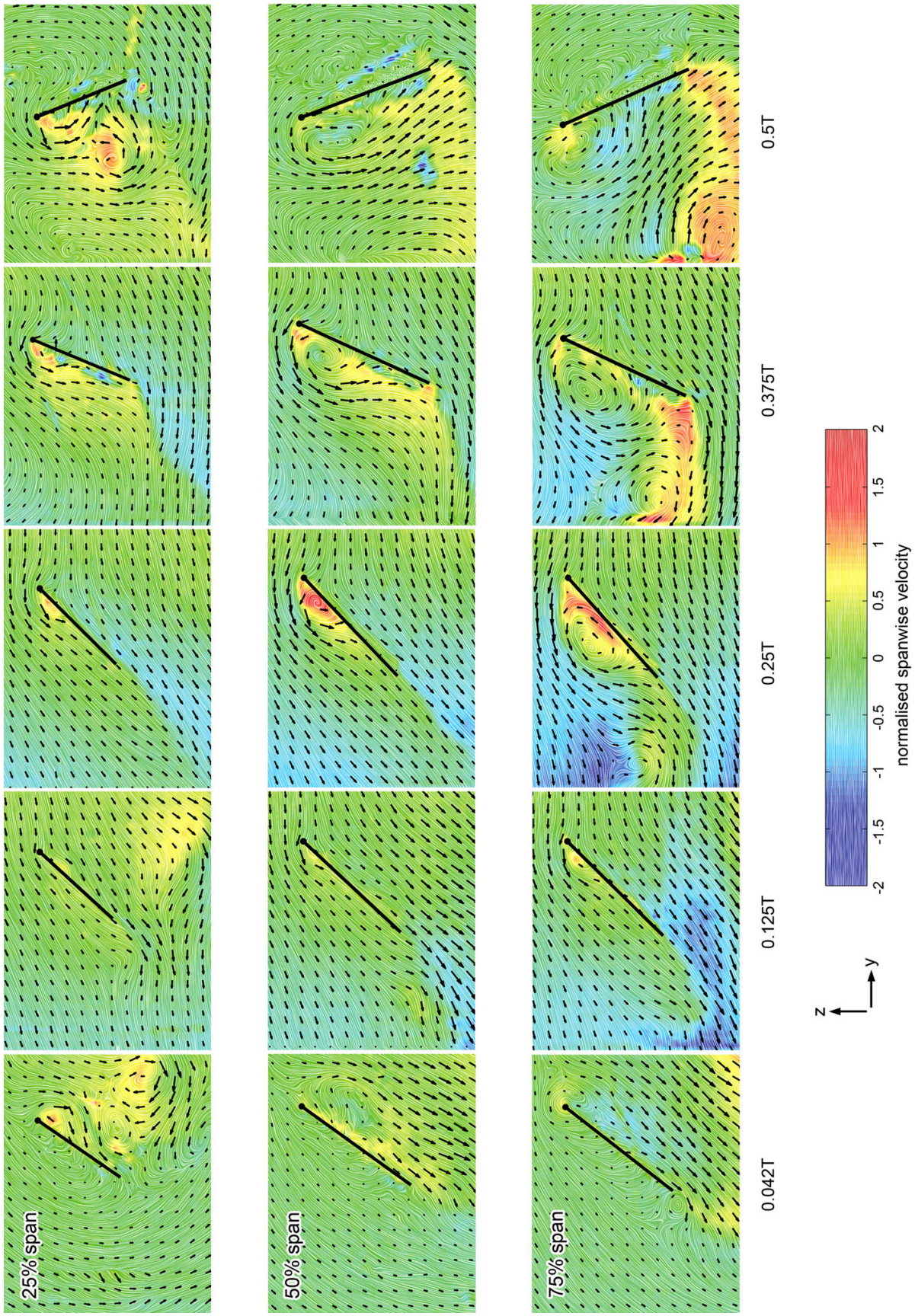

Figure 10: Chordwise planes at 25%, 50% and 75% span throughout the flapping half cycle illustrating undersampled vector maps overlaid on LIC images coloured with spanwise velocity normalised with respect to the mean wingtip speed

mid-span in experiments by Lu and Shen [10] and by Lentink and Dickinson [20]. Vortex breakdown occurs when a stagnation point is present on the vortex axis followed by a region of reversed flow [39]. In this case, vortex breakdown probably occurs because the primary LEV spiralling towards the tip encounters root-ward flow originating from the tip vortex, creating a stagnation point between the two flows. It was postulated by Liu et al. [40] that breakdown of the LEV resulted from an adverse pressure gradient originating from flow from the tip vortex. The observed sudden growth in vortex diameter is also illustrated in Fig. 10 by comparing the size of the LEV outboard at $0.125T$ where the LEV is very small versus that at $0.25T$ where the LEV appears to extend over most of the wing chord.

Interestingly, at $0.208T$ and $0.25T$ the iso-surface of $Q = 6 \times 10^6 s^{-2}$ suddenly disappears around the same location where the spanwise flow suddenly drops and the vortex core diameter increases. This sudden drop in Q value indicates that the primary LEV transitions from a rigid-body-like rotation to a state with comparatively higher strain rates. This makes sense in view of the fact that this vortex suddenly expands beyond the breakdown location, where by conservation of angular momentum the spiralling fluid with a tight radius from the root must decrease in angular velocity as the radius suddenly expands. Thus, the rotation rates in the fluid go down with angular velocity and the strain rates become comparatively larger which means a lower Q value.

Moving to Fig. 9, it can be seen that beyond $0.25T$ the vortex breakdown location moves inboard as the sweep progresses, as indicated by the decrease in spanwise flow through the core of the primary LEV. This decrease in spanwise flow through the LEV core beyond $0.25T$ is also visible in Fig. 10 from mid-span to the outboard regions. It can also be seen in Fig. 9 between $0.292T$ and $0.375T$ that as the wing decelerates, the tip vortex's axial direction with respect to the wing switches from being directed away from the wing to being directed towards the wing. This switch occurs somewhere around $0.333T$, and results from the fact that as the wing decelerates, the wing sees the tip vortex more and more as it is seen with respect to the ground. Here, an observer fixed to the ground sees the tip vortex with an axial velocity directed towards the wing. Thus, as the wing comes to rest, portions of the tip vortex which were shed slightly earlier in the stroke begin to catch up with the wing. As the tip vortex flows into the wing and pitch reversal occurs, the tip vortex increases in diameter, as illustrated in Fig. 11 (this increase is also confirmed upon examining the tip vortex tangential velocity profiles), and the spanwise flow through the primary LEV decreases even further as it has a more prominent negative spanwise flow originating from the tip vortex to compete with. Despite this, the primary LEV remains attached to the wing surface until the end of the flapping half cycle at $0.5T$ when the wing has come to rest and the previous wing topside has become the underside. After this, the process repeats as the wing progresses into the subsequent flapping half cycle. It

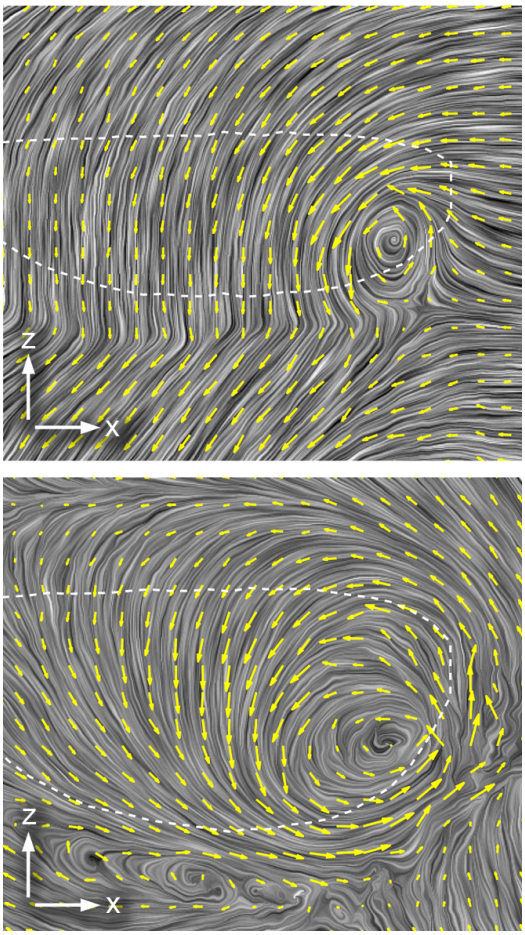

Figure 11: xz planes of undersampled vectors approximately $0.9\bar{c}$ behind the wing pitch axis illustrating the tip vortex size at $0.25T$ (top) and $0.417T$ (bottom); the wing outline is shown by the white dashed line

should be noted that here the LEV is considered to be attached in the sense that, although it shifts towards the trailing edge at the outboard regions as the stroke progresses (i.e. compare top views at $0.042T$ to $0.25T$ in Fig. 8), it was always observed to be present over the wing surface and was not seen to convect away from the wing into the wake.

10 Conclusions

The flow around an insect-like flapping-wing throughout a flapping half cycle was measured and visualised to reveal how the LEV and spanwise flow forms and evolves. It was seen that the beginning of a flapping half cycle is characterised by the formation of a starting vortex at the trailing edge, a tip vortex, and a primary LEV towards the tip, while the primary LEV from the previous half-stroke still persists under the wing. As the half-stroke progresses and the primary LEV shifts towards the trailing edge, a secondary LEV appears to form along the leading edge. The primary LEV grows in size as the flapping half cycle continues, and the level of spanwise flow through its core increases to a maximum of approximately two times the mean wingtip speed at the mid-stroke position where the primary LEV suddenly increases in size outboard and shows signs of breakdown around 65% span. Beyond mid-stroke, the spanwise flow through the core of the primary LEV decreases and the breakdown location shifts inboard. As the wing decelerates and pitch reversal occurs the axial direction of the tip vortex reverses, resulting in an increase in the size of the tip vortex as it flows into the wing and a further decrease in spanwise flow in the primary LEV. At the end of the half-stroke the primary LEV is still present over the wing surface. Since the LEV was observed to be present over the wing surface and not fall away into the wake throughout the entire flapping half cycle, the LEV was considered to be attached to the wing.

Acknowledgements

The authors would like to thank Professor Rafał Żbikowski for his guidance on data reduction and other contributions to the setup of this investigation; and Dr. Graham Stabler for his help and advice in the development of the experimental apparatus. The first author (NP) was partially supported by an Overseas Research Students Award during this work.

References

[1] Żbikowski, R., "Flapping wing autonomous micro air vehicles: research programme outline," *Fourteenth International Conference on Unmanned Air Vehicle Systems*, Vol. Supplementary Papers, 12-14 April 1999, pp. 38.1–38.5.

[2] Woods, M. I., Henderson, J. F., and Lock, G. D., "Energy requirements for the flight of micro air vehicles," *Aeronautical Journal*, Vol. 105, No. 1043, March 2001, pp. 135–149.

[3] Ellington, C. P., van den Berg, C., Willmott, A. P., and Thomas, A. L. R., "Leading-edge vortices in insect flight," *Nature*, Vol. 384, 19/26 December 1996, pp. 626–630.

[4] van den Berg, C. and Ellington, C. P., "The vortex wake of a "hovering" model hawkmoth," *Philosophical Transactions of the Royal Society of London Series B*, Vol. 352, No. 1351, 29 March 1997, pp. 317–328.

[5] van den Berg, C. and Ellington, C. P., "The three-dimensional leading-edge vortex of a "hovering" model hawkmoth," *Philosophical Transactions of the Royal Society of London Series B*, Vol. 352, No. 1351, 29 March 1997, pp. 329–340.

[6] Birch, J. M. and Dickinson, M. H., "Spanwise flow and the attachment of the leading-edge vortex on insect wings," *Nature*, Vol. 412, No. 6848, 2001, pp. 729–733.

[7] Bomphrey, R. J., Lawson, N. J., Harding, N. J., Taylor, G. K., and Thomas, A. L. R., "The aerodynamics of *Manduca sexta*: digital particle image velocimetry analysis of the leading-edge vortex," *Journal of Experimental Biology*, Vol. 208, 2005, pp. 1079–1094.

[8] Bomphrey, R. J., Lawson, N. J., Taylor, G. K., and Thomas, A. L. R., "Application of digital particle image velocimetry to insect aerodynamics: measurement of the leading-edge vortex and near wake of a hawkmoth," *Experiments in Fluids*, Vol. 40, No. 4, 2006, pp. 546–554.

[9] Poelma, C., Dickson, W. B., and Dickinson, M. H., "Time-resolved reconstruction of the full velocity field around a dynamically-scaled flapping wing," *Experiments in Fluids*, Vol. 41, 2006, pp. 213–225.

[10] Lu, Y. and Shen, G. X., "Three-dimensional flow structures and evolution of the leading-edge vortices on a flapping wing," *Journal of Experimental Biology*, Vol. 211, No. 8, 2008, pp. 1221–1230.

[11] Dickinson, M. H., Lehmann, F.-O., and Sane, S. P., "Wing rotation and the aerodynamic basis of insect flight," *Science*, Vol. 284, No. 5422, 18 June 1999, pp. 1954–1960.

[12] Willmott, A. P. and Ellington, C. P., "The mechanics of flight in the hawkmoth Manduca sexta: I. kinematics of hovering and forward flight," *Journal of Experimental Biology*, Vol. 200, 1997, pp. 2705–2722.

[13] Ansari, S. A., *A nonlinear, unsteady, aerodynamic model for insect-like flapping wings in the hover with micro air vehicle applications*, Ph.D. thesis, Cranfield University (Shrivenham), September 2004.

[14] Bomphrey, R. J., "Insects in flight: direct visualization and flow measurements," *Bioinspiration & Biomimetics*, Vol. 1, 2006, pp. 1–9.

[15] Wilkins, P. C., *Some unsteady aerodynamics relevant to insect-inspired flapping-wing micro air vehicles*, Ph.D. thesis, Cranfield University (Shrivenham), June 2008, http://hdl.handle.net/1826/2913.

[16] Phillips, N., *Experimental unsteady aerodynamics relevant to insect-inspired flapping-wing micro air vehicles*, Ph.D. thesis, Cranfield University (Shrivenham), April 2011, http://hdl.handle.net/1826/5824.

[17] Maxworthy, T., "Experiments on the Weis-Fogh mechanism of lift generation by insects in hovering flight. part 1: dynamics of the 'fling'," *Journal of Fluid Mechanics*, Vol. 93, 1979, pp. 47–63.

[18] Wilkins, P. C. and Knowles, K., "The leading-edge vortex and aerodynamics of insect-based flapping-wing micro air vehicles," *Aeronautical Journal*, Vol. 113, No. 1143, 2009, pp. 253–262.

[19] Usherwood, J. R. and Ellington, C. P., "The aerodynamics of revolving wings I. model hawkmoth wings," *Journal of Experimental Biology*, Vol. 205, 2002, pp. 1547–1564.

[20] Lentink, D. and Dickinson, M. H., "Rotational accelerations stabilize leading edge vortices on revolving fly wings," *Journal of Experimental Biology*, Vol. 212, 2009, pp. 2705–2719.

[21] Tarascio, M. J., Ramasamy, M., Chopra, I., and Leishman, J. G., "Flow visualization of micro air vehicle scaled insect-based flapping wings," *Journal of Aircraft*, Vol. 42, No. 2, March–April 2005, pp. 385–390.

[22] Jones, A. and Babinsky, H., "Unsteady lift generation on rotating wings at low Reynolds numbers," *Journal of Aircraft*, Vol. 47, No. 3, 2010, pp. 1013–1021.

[23] Jones, A. and Babinsky, H., "Reynolds number effects on leading edge vortex development on a waving wing," *Experiments in Fluids*, Vol. 51, No. 1, 2011, pp. 197–210.

[24] Thomas, A. L. R., Taylor, G. K., Srygley, R. B., Nudds, R. L., and Bomphrey, R. J., "Dragonfly flight: free-flight and tethered flow visualizations reveal a diverse array of unsteady lift-generating mechanisms, controlled primarily via angle of attack," *Journal of Experimental Biology*, Vol. 207, 2004, pp. 4299–4323.

[25] Phillips, N. and Knowles, K., "Progress in the development of an adjustable, insect-like flapping-wing apparatus utilising a three degree-of-freedom parallel spherical mechanism," *International Powered Lift Conference*, Royal Aeronautical Society, London, UK, 22-24 July 2008.

[26] Galiński, C. and Żbikowski, R., "Materials challenges in the design of an insect-like flapping wing mechanism based on a four-bar linkage," *Materials & Design*, Vol. 28, No. 3, 2007, pp. 783–796.

[27] Pedersen, C. B., *An indicial-Polhamus model of aerodynamics of insect-like flapping wings in hover*, Ph.D. thesis, Cranfield University (Shrivenham), 17 June 2003.

[28] Lawson., N. J. and Wu, J., "Three-dimensional particle image velocimetry: error analysis of stereoscopic techniques," *Measurement Science and Technology*, Vol. 8, 1997, pp. 894–900.

[29] Prasad, A. K., "Stereoscopic particle image velocimetry," *Experiments in Fluids*, Vol. 29, 2000, pp. 103–116.

[30] Raffel, M., Willert, C., and Kompenhans, J., *Particle image velocimetry: a practical guide*, Springer-Verlag, Berlin, 1998.

[31] Lu, Y., Shen, G. X., and Lai, G. J., "Dual leading-edge vortices on flapping wings," *Journal of Experimental Biology*, Vol. 209, 2006, pp. 5005–5016.

[32] Westerweel, J., "Efficient detection of spurious vectors in particle image velocimetry data," *Experiments in Fluids*, Vol. 16, 1994, pp. 236–247.

[33] Willert, C. E., "Stereoscopic digital particle image velocimetry for application in wind tunnel flows," *Measurement Science and Technology*, Vol. 8, 1997, pp. 1465–1479.

[34] Scarano, F., David, L., Bsibsi, M., and Calluaud, D., "S-PIV comparative assessment: image dewarping+misalignment correction and pinhole+geometric back projection," *Experiments in Fluids*, Vol. 39, 2005, pp. 257–266.

[35] Knowles, R. D., Finnis, M. V., Saddington, A. J., and Knowles, K., "Planar visualization of vortical flows," *Proceedings of the Institution of Mechanical Engineering, Part G: Journal of Aerospace Engineering*, Vol. 220, No. 6, 2006, pp. 619–627.

[36] Hunt, J. C. R., Wray, A. A., and Moin, P., "Eddies, stream, and convergence zones in turbulent flows," Tech. rep., Center for Turbulence Research, 1988, Report CTR-S88.

[37] Willert, C. E. and Gharib, M., "Digital particle image velocimetry," *Experiments in Fluids*, Vol. 10, 1991, pp. 181–193.

[38] Srygley, R. B. and Thomas, A. L. R., "Unconventional lift-generating mechanisms in free-flying butterflies," *Nature*, Vol. 420, December 2002, pp. 660–664.

[39] Leibovich, S., "Vortex stability and breakdown: survey and extension," *AIAA Journal*, Vol. 22, No. 9, September 1984, pp. 1192–1206.

[40] Liu, H., Ellington, C. P., Kawachi, K., van den Berg, C., and Wilmott, A. P., "A computational fluid dynamic study of hawkmoth hovering," *Journal of Experimental Biology*, Vol. 201, 1998, pp. 461–477.